

Accepted Manuscript

Robust demarcation of basal cell carcinoma by dependent component analysis-based segmentation of multi-spectral fluorescence images

Ivica Kopriva, Antun Peršin, Neira Puizina-Ivić, Lina Mirić

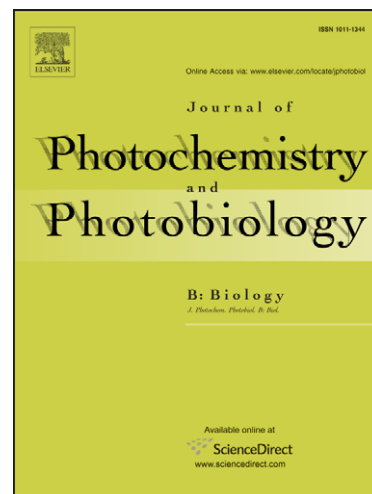
PII: S1011-1344(10)00076-X
DOI: [10.1016/j.jphotobiol.2010.03.013](https://doi.org/10.1016/j.jphotobiol.2010.03.013)
Reference: JPB 9024

To appear in: *Journal of Photochemistry and Photobiology B: Biology*

Received Date: 23 April 2009
Revised Date: 12 March 2010
Accepted Date: 30 March 2010

Please cite this article as: I. Kopriva, A. Peršin, N. Puizina-Ivić, L. Mirić, Robust demarcation of basal cell carcinoma by dependent component analysis-based segmentation of multi-spectral fluorescence images, *Journal of Photochemistry and Photobiology B: Biology* (2010), doi: [10.1016/j.jphotobiol.2010.03.013](https://doi.org/10.1016/j.jphotobiol.2010.03.013)

This is a PDF file of an unedited manuscript that has been accepted for publication. As a service to our customers we are providing this early version of the manuscript. The manuscript will undergo copyediting, typesetting, and review of the resulting proof before it is published in its final form. Please note that during the production process errors may be discovered which could affect the content, and all legal disclaimers that apply to the journal pertain.



**Robust demarcation of basal cell carcinoma by dependent component analysis-based
segmentation of multi-spectral fluorescence images**

Ivica Kopriva^{a*}, Antun Peršin^a, Neira Puizina-Ivić^b, Lina Mirić^b

^aDivision of Laser and Atomic Research and Development, Ruđer Bošković Institute,
Bijenička cesta 54, P.O. Box 180, 10002, Zagreb, Croatia

^bClinic of Dermatovenerology, Clinical Hospital and School of Medicine, Šoltanska 1, 21000
Split

e-mail: ikopriva@irb.hr, persin@irb.hr, neira.puizina@kbsplit.hr, lina.miric@gmail.com

phone: +385-1-4571-286

fax: +385-1-4680-104

Abstract

This study was designed to demonstrate robust performance of the novel dependent component analysis (DCA)-based approach to demarcation of the basal cell carcinoma (BCC) through unsupervised decomposition of the red-green-blue (RGB) fluorescent image of the BCC. Robustness to intensity fluctuation is due to the scale invariance property of DCA algorithms, which exploit spectral and spatial diversities between the BCC and the surrounding tissue. Used filtering-based DCA approach represents an extension of the independent component analysis (ICA) and is necessary in order to account for statistical dependence that is induced by spectral similarity between the BCC and surrounding tissue. This generates weak edges what represents a challenge for other segmentation methods as well. By comparative performance analysis with state-of-the-art image segmentation methods such as active contours (level set), K-means clustering, non-negative matrix factorization,

ICA and ratio imaging we experimentally demonstrate good performance of DCA-based BCC demarcation in two demanding scenarios where intensity of the fluorescent image has been varied almost two-orders of magnitude.

Key words: basal cell carcinoma, photodynamic detection, dependent component analysis, tumor demarcation, multi-spectral image.

1. Introduction and objectives

Among the skin tumors, basal cell carcinoma (BCC) accounts for about 80% of all non-melanoma skin cancers [1]. Increased occurrence of the skin cancer all over the world, [2], implies the large need for complementary methods for detection and accurate demarcation of these skin cancers at an early stage to limit the damage caused by the tumors [3]. Photodynamic diagnoses (PDD) is a method for tumor demarcation that is based on the visualization of a fluorophore, with the ability to accumulate in tumor tissue, by the use of fluorescence imaging. A photosensitizer widely used in clinical applications is δ -5 aminolevulinic acid (ALA) induced protoporphyrin IX (PpIX) [1,4-9]. ALA is a non-fluorescent precursor of fluorescent PpIX, with a degree of selective accumulation shown in a variety of malignancies [10]. Thus, by using suitable intensity excitation light, the PpIX can be located in the tissue by virtue of its fluorescence. Visualization of the PpIX represents the basis of the PDD of the skin tumors and has been exploited in the design of the fluorescence imaging systems [1,3,11-16].

Image processing methods widely used for demarcation of the BCC after administration with ALA induced PpIX are ratio imaging method [1,11,13], and threshold based imaging [3]. As it has been previously demonstrated in [17], accuracy of both methods for tumor demarcation depends essentially on the optimality of the threshold that up to some

extent is defined heuristically. When intensity of the fluorescence is fluctuating the threshold based methods will introduce errors in tumor demarcation, what has been demonstrated in [17]. However, robustness of tumor demarcation methods with respect to intensity fluctuation should be of the interest in the early stages of the tumor development, in which case detection and accurate demarcation is of special importance. At this stage, in order to avoid possibility of misunderstanding, we would like to emphasize difference between tumor demarcation (that is main objective of this paper) and tumor diagnoses. In tumor demarcation we are interested in accurate calculation of the tumor boundaries i.e. tumor localization [10]. This is achieved by means of various image segmentation algorithms [3, 11-18]. On the other side the purpose of (noninvasive) tumor diagnoses is identification of and differentiation between various types of tumors, [19-22]. In [19, 21, 22] multispectral imaging systems were used for the purpose of noninvasive tumor diagnoses with spectral resolution significantly higher than in the case of the RGB image.

As pointed out in [3], in order to obtain a reliable contrast between tumor and normal skin in PDD, it is desirable to keep the fluorescence variation in ALA treated normal skin as low as possible. In the comprehensive study conducted in [3] it has been demonstrated that optimal contrast is achieved when ALA application time is in the range 3-4 h. In such a case it is possible to define optimal threshold and classify as BCC everything that is above cI_a , where I_a represents average intensity of the region with healthy skin, and c represents factor that has been empirically found to be $c \approx 1.4$ for 3-4 h of ALA application, [3]. In our study we have adopted different approaches to achieve robust tumor demarcation: derivation of novel unsupervised image segmentation methods the performance of which remains invariant under wide range of the variability of the fluorescence intensity. Variation of the fluorescence intensity can be caused by several factors, either individually or combined:

duration of the ALA application time, quality/concentration of the ALA cream and/or intensity of the illuminating light.

In [17] unsupervised decomposition of the red-green-blue (RGB) fluorescent image has been performed by using independent component analysis (ICA) [23,24] for the purpose of BCC demarcation. ICA is relatively old theory derived over last almost 20 years for unsupervised analysis of the multivariate data sets. Of the interest for tumor demarcation is the capability of ICA algorithms for unsupervised segmentation of multi-spectral and hyper-spectral images [25-27]. Unsupervised segmentation by ICA is based on assumption of statistical independence among the objects present in the multi-spectral fluorescent image of the tumor, where BCC is one object and surrounding healthy tissue is another object. Because statistical independence is scale invariant, it is expected that ICA will be robust with respect to the variation of the intensity level.

The linear mixture model (LMM), introduced in section 2.3, as a representation of the multi-spectral image has this paper the following interpretation: columns of the basis matrix represent spectral profiles of the materials present in the image, while rows of the source matrix represent spatial distributions of the materials. That is why blind source separation methods when applied to LMM of the multi-spectral image perform its segmentation. As discussed in more details in section 2.3, adopted interpretation implies that spectrally similar materials will also have partially statistically dependent spatial distributions. As opposed to this interpretation, approaches to blind spectral unmixing such as [27-29] are based on the following interpretation of the LMM of the multi-spectral and/or hyperspectral image: columns of the basis matrix are reflectance of the materials and columns of the source matrix are fractional abundances representing the percentage of the pixel footprint occupied by each material. Because sum of the fractional abundances must be one, this sum-to-one constraint implies their statistical dependence. Following our interpretation of the LMM, we shall

demonstrate that for the low-dimensional multi-spectral images, such as RGB image for example, statistical independence assumption among the spatial distributions of the objects present in the image scene is violated due to the partial overlapping of the spectra of the objects. Thus, coarse spectral resolution of the RGB image causes partial statistical dependence between the objects in the spatial domain and deteriorates performance of the ICA-based approach to tumor demarcation problem. In this paper we apply filtering-based dependent component analysis (DCA), [30-36], to fix the statistical dependence problem systematically. This is achieved combining the high-pass filtering like linear preprocessing transform and ICA in transformed domain where statistical independence among the objects present in the fluorescent multi-spectral image is increased. High-pass filtering based DCA selected is selected due the known empirical fact, [24, 35, 37], that it is the low-frequency part of the source spectrum that is responsible for statistical dependence among the sources. The main objective of this paper is experimental demonstration of the capability of the proposed DCA-based multi-spectral image decomposition to yield an accurate estimate of the tumor demarcation line under high degree of variability of the intensity of the fluorescent image. This should lay down foundation for the design of the autonomous systems capable for robust calculation of the tumor demarcation lines in the real world clinical conditions.

2. Materials and methods

2.1 Patients

Patients with histologically verified diagnoses of superficial multicentric basal cell carcinomas in the lower right part of the back were admitted in Outpatient department of dermatovenerology in the Clinic of Dermatovenerology, Clinical Hospital Split. The study protocol, patient information and consent forms were approved by an independent ethics committee before patients were enrolled in the study. The ALA cream was prepared at the

hospital pharmacy. It consisted of 20% 5-ALA-HCl (Medac, Hamburg, Germany) in an ointment base (Belobaza, Belupo, Koprivnica, Croatia), 2% of dimethylsulfoxide (DMSO) and 2% of edetic acid disodium salt (EDTA) (Titriplex III, Merck, Germany). The cream was prepared daily just prior the application. After cleaning the area with a saline solution, the cream has been applied to a thickness of approximately 1 mm covering the treated area and 1 cm of the surrounding skin. The area was covered by plastic occlusive dressing (Tegaderm, 3M, UK) and an aluminum foil on the top in order to protect treated skin from exposure to environment light. The size of the treated area was in the range 3x3 cm. Before imaging, the occlusive dressing was removed and cream was wiped off gently with gauze. After imaging, disinfection of treated area was done and demarcation line was marked by tissue marking dye (TBS, Triangle Biomedical Sciences, Inc., Durham, NC, USA). Thereafter, surgical excision was obtained and specimens were fixed in 10% formalin and sent in the Laboratory for dermatopathology.

2.2 Fluorescence imaging

Fluorescence imaging has been performed by apparatus consisting of commercial RGB digital camera with precise manual focusing capability and illuminator. Illuminator is based on the cluster of light emitting diodes arranged circularly around camera lens and emitting in the range of 405 nm, which matches the absorption spectrum of PpIX. The fluorescence emission spectrum of PpIX has a dominant peak at 635 nm. Both spot diameter and fluorescence intensity can be adjusted independently in the range of 2 to 100 cm and 0.01 to 100 mw/cm², respectively. Depending on spot size and intensity applied, exposure time for capturing fluorescence images ranges from 0.01 to 10 sec. The camera produced 24-bit RGB

colored image (8 bits per color) with spatial resolution of 2352 x 3136 pixels. Because the projection of the field of view on the skin of the patients was approximately 10 x 10 cm this yielded the pixel footprint of approximately 0.0014 mm² i.e. the spatial resolution in the experimental setup was extremely fine.

2.3 Multi-spectral imaging

RGB image is a multi-spectral image with the coarse spectral resolution. It is suitable for the application of the multivariate data analysis methods such as ICA and DCA in order to achieve unsupervised extraction of the BCC spatial map. This holds true as long as the fluorescent image consists of three or less objects. For the sake of illustration Figures 1a to 1c show RGB fluorescent image of the BCC acquired under different intensities of illumination with 405 nm light. For the segmentation purpose multi-spectral image is represented in a form of the LMM [17, 25, 26, 38-41]

$$\mathbf{X}=\mathbf{A}\mathbf{S} \quad (1)$$

where $\mathbf{X} \in \mathbb{R}_{0^+}^{N \times T}$ represents multi-spectral image consisting of N spectral bands and $T=P \times Q$ pixels, $\mathbf{A} \in \mathbb{R}_{0^+}^{N \times M}$ represents basis or mixing matrix and $\mathbf{S} \in \mathbb{R}_{0^+}^{M \times T}$ represents matrix of the M objects or classes present in the image scene. Each row of \mathbf{X} and \mathbf{S} is a signal or 1D image representation obtained from its 2D counterpart by some 2D \rightarrow 1D mapping. Most common type of mapping is the column- or row-stacking procedure also called vectorization. Because we are concerned with an unsupervised image decomposition problem, we assume \mathbf{X} , \mathbf{A} and \mathbf{S} to be nonnegative.

Representation of multi-spectral image with LMM (1) converts image segmentation problem into LMM decomposition problem. When mixing matrix \mathbf{A} is known decomposition problem is efficiently solved on supervised way through the least-squares approach. However, in a number of real world problems it is impossible to know the mixing matrix \mathbf{A} , in which case decomposition problem must be solved in unsupervised manner. This is quite a challenging problem because both mixing matrix \mathbf{A} and object matrix \mathbf{S} must be estimated having at disposal multi-spectral image matrix \mathbf{X} only.

The LMM (1) is widely used in multi-spectral and hyper-spectral remote sensing where 3D image cube contains co-registered spectral images of the same scene. Within this application field, N represents the number of spectral bands; rows $\{\mathbf{x}_n\}_{n=1}^N$ of \mathbf{X} represent spectral images, and columns of \mathbf{X} represent multi-spectral pixel vectors at particular spatial locations, $t \leq T$, in the image; T represents the number of pixels in the image, column vectors $\{\mathbf{a}_m\}_{m=1}^M$ of the basis matrix \mathbf{A} represent spectral responses of the materials present in the image, while rows of \mathbf{S} represent spatial distributions of these materials. Assuming that \mathbf{X} represents an RGB image the number of spectral bands equals $N=3$. Adopted interpretation of the LMM (1) converts image segmentation problem to blind source separation problem. Following this interpretation we immediately see that spectral similarity of the objects \mathbf{s}_m and \mathbf{s}_n will affect the condition number of the basis matrix, because the corresponding column vectors \mathbf{a}_m and \mathbf{a}_n become collinear. When the objects have the same spectral responses the column rank of the basis matrix is less than the number of objects M . Moreover, the corresponding objects become statistically dependent. This is easily verified by assuming that two objects \mathbf{s}_m and \mathbf{s}_n are spectrally very similar. Then $\mathbf{a}_n \cong c\mathbf{a}_m$, where c represents the intensity scaling factor. The contribution of these two objects at any pixel location t is: $\mathbf{a}_m s_{mt} + \mathbf{a}_n s_{nt} \cong \mathbf{a}_m s_{mt} + \mathbf{a}_m c s_{nt}$, implying that \mathbf{s}_m and $c\mathbf{s}_n$ are indistinguishable, i.e., \mathbf{s}_m and \mathbf{s}_n are statistically dependent. Hence, fundamental requirement imposed by the ICA algorithms on

the LMM fails when materials, tumor and surrounding healthy tissue, become spectrally similar. This occurs for example when tumor is at an early stage of development. This spectral similarity problem presents a motivation to look for an extension of the basic ICA theory in order to achieve more accurate blind segmentation/separation of statistically dependent objects. As opposed to adopted interpretation of the LMM (1) approaches to blind spectral unmixing described in [27-29] presume that columns of the basis matrix are reflectance of the materials and columns of the source matrix are fractional abundances representing the percentage of the pixel footprint occupied by each material. Since sum of the fractional abundances must be one, it implies that sources (fractional abundances) are statistically dependent. Filtering-based DCA used in this paper is not capable to take into account sum-to-one constraint but is suitable to remove low-frequency part of the source spectra that causes dependence between the sources (spatial distributions of the materials present in the image).

2.4 Dependent component analysis

The basic idea behind ICA is to decompose a set of multivariate signals into a basis of statistically independent sources with the minimal loss of information content so as to achieve detection and classification. In the unsupervised segmentation problem, which for the case of multi-spectral image is represented by LMM (1), this implies estimation of the spectral reflectance matrix \mathbf{A} and materials spatial distributions matrix \mathbf{S} having at disposal multi-spectral image \mathbf{X} only. As already said, ICA solves related BSS problem under three assumptions made on the unknown source signals $\{\mathbf{s}_m\}_{m=1}^M$: 1) each source signal is an independent identically distributed (i.i.d.) stationary random process; 2) the source signals are statistically independent at any position; and 3) at most one among the source signals has

Gaussian distribution. The mixing matrix \mathbf{A} although unknown is also assumed to be non-singular. Then, the solution to the blind source separation problem (BSS) is obtained with the scale and permutation indeterminacy, i.e., $\mathbf{W}\mathbf{A} = \mathbf{P}\mathbf{\Lambda}$, where \mathbf{W} represents the unmixing matrix, \mathbf{P} is a generalized permutation matrix, and $\mathbf{\Lambda}$ is a diagonal matrix. These requirements ensure the existence and uniqueness of the solution to the BSS problem up to the ordering, sign and scale, [23,24]. Thus, ICA algorithms possess the scale invariance property what makes them attractive for the use in demarcation of the BCC from the RGB fluorescence image when the absolute fluorescence level may vary from measurement to measurement.

However, we have shown that spectral similarity between the materials present in the multi-spectral image induces statistical dependence among them. Thus, one of the basic assumptions upon which the ICA theory is built on, statistical independence among the objects, is violated when they become spectrally similar. Filtering-based DCA represents an extension of the ICA in the solution of the BSS problem with statistically dependent sources. The strategy behind filtering-based DCA is to find a linear transform T that improves statistical independence between the sources \mathbf{S} in transformed domain, i.e.

$$T(\mathbf{X}) = T(\mathbf{A}\mathbf{S}) \cong \mathbf{A}T(\mathbf{S}) \quad (2)$$

Since low-frequency part of the source spectrum is responsible for dependence among the sources, [24, 35, 37], linear transform is expected to behave as high-pass filter. Examples of such transform are: high-pass filtering (HPF), [35]; innovation (Inn), [31]; low-pass filtering with variable size [32], and wavelet transforms (WT), [33, 34]. HPF can be seen as a special case of the innovations based preprocessing, wherein innovations provide data adaptive filtering. Data adaptive filtering makes innovations an optimal choice for filtering-based

DCA. Arguments for using innovations (prediction errors) are that they are more independent and more non-Gaussian than original processes. This is of essential importance for the use of ICA after innovations-based filtering. The innovation process is defined as prediction error:

$$\tilde{s}_m(t) = s_m(t) - \sum_{l=1}^L b_{ml} s_m(t-l) \quad m = 1, \dots, M \quad (3)$$

where \mathbf{b}_m is the vector of prediction coefficients. $\tilde{s}_m(t)$ represents new information that $s_m(t)$ has but is not contained in the past L samples. When innovations representation (3) is applied row-wise to the LMM (1) it follows

$$\tilde{\mathbf{X}} = \mathbf{A}\tilde{\mathbf{S}} \quad (4)$$

However, it has been already demonstrated in [24,31,33], that computationally very simple first order differentiator with the impulse response $h=[1 \ -1]$ yields good performance in the image processing-type of applications. It can be seen as a first order innovation process and has been used in our implementation of the HPF-based DCA algorithm in the experiments reported in Section 3.

Because the sources in the new representation space will be less statistically dependent, any ICA algorithm derived for the original BSS problem represented by the LMM (1), can be used to learn the basis matrix \mathbf{A} . Once the basis matrix \mathbf{A} is estimated, the sources \mathbf{S} are recovered by applying the pseudo-inverse of \mathbf{A} on the multi-spectral image \mathbf{X} in (1). In our experiments we have used enhanced version, [42], of the FastICA algorithm, [43, 44] due to its property of being asymptotically statistically efficient.

Nonnegative matrix factorization (NMF) algorithms, [45-48], can be viewed as a special class of the DCA algorithms, because they are also applicable to the LMM (1) since the variables in the model are nonnegative. The NMF algorithms do not impose statistical independence and non-Gaussianity requirements on the sources. However, NMF algorithms generally require $N \gg M$. This makes them not good candidate for unsupervised decomposition problems when \mathbf{X} represents a low-dimensional multi-spectral image, such as RGB image, in which case N is small. Moreover, NMF algorithms without additional constraints imposed on the sources (the most often used constraints is sparseness) produce factorization that is not unique, [46,48]. Using a gradient descent approach to NMF yields multiplicative NMF algorithms [45,46,48]. They are known to be very slowly convergent and easily get stuck in local minima. Therefore, in [47] an algorithm was recently derived that is based on the use of second-order terms, Hessian, in the Taylor expansion of a cost function to speed up convergence. Specifically, the NMF algorithm used in the experiments in the cited paper combines quasi-Newton optimization for basis matrix \mathbf{A} and a fixed-point regularized least-square algorithm for \mathbf{S} , with computer code provided in the appendix in [47]. Excellent performance of this algorithm has been in [46,47]. We have used this NMF algorithm in the comparative experimental performance analysis presented in Section 3. Despite the fact that no hard constraints were imposed on the sources this NMF method yielded meaningful result, that however was inferior in relation to the one obtained by HPF-based DCA algorithm.

3. Results

In study conducted in this paper we have proposed unsupervised tumor demarcation method the performance of which remains invariant under wide range of the variability of the fluorescence intensity. To verify performance of various tumor demarcation methods we have illuminated BCC on two patients with different intensity levels ranging from some

reference level I_0 to the level $I_0/73.47$ in the case of first patient, i.e. from reference level I_0 to the level $I_0/58.67$ in the case of second patient. Figures 1a to 1c show fluorescent RGB images of the BCC of the first patient. Images were acquired after illumination with the intensity I_0 , Figure 1a; intensity $I_0/9.15$, Figure 1b; and intensity $I_0/73.47$, Figure 1c. Figure 1d shows RGB image of the same tumor with demarcation line marked by red dots. Figures 10a to 10c show fluorescent RGB images of the BCC of the second patient. Images were acquired after illumination with the intensity I_0 , Figure 10a; intensity $I_0/12.22$, Figure 1b; and intensity $I_0/58.67$, Figure 10c. Through biopsy, described in Section 2.1, it has been verified that there is no tumor outside of the region marked by red dots. Thus, Figure 1d can serve as a reference in comparative performance analysis of the tumor demarcation methods. The biopsy procedure has been also performed on the tumor of the second patient.

Figures 2a to 2c present histograms of the grayscale images obtained from RGB images shown in Figures 1a to 1c by MATLAB command `rgb2gray`. Evidently, not full dynamic range of the camera has been used. However, it was our intention to verify the robustness of the segmentation methods with respect to fluctuation of the intensity of fluorescence without having any external interfering factor. Therefore, once the camera was adjusted the setup was fixed while images were acquired after intensity of the illuminating light has been varied.

In addition to NMF, ICA, filtering-based DCA and ratio-imaging algorithms we have also tested state-of-the-art intensity based image segmentation methods. Representatives of this class of methods are active contour or level set methods [49-52] and clustering-based methods [53, 54]. In particular we have tested recently derived level set algorithm, [52], that exhibits robust performance in the presence of weak boundaries and K-means clustering algorithm [54]. A computer code for the MATLAB implementation of the level set algorithm [53] has been downloaded from [55] under category: image segmentation. In the

initialization of the K-means algorithm we have used *a priori* information about number of clusters to be 2. We have applied level set and K-means algorithm on gray scale version of the RGB image shown in Figure 1a, and ratio imaging method [1,11,13] on the fluorescence RGB image. We remind that Figure 1a has been acquired under illumination with maximal intensity. Figure 3 shows evolution curve estimated by the level set algorithm [52, 55] after 700 iterations and superimposed on the gray scale version of the Figure 1a. Although the contrast on the original image was maximal, in comparison to other acquired fluorescent images, the method failed to converge toward tumor boundaries. Figures 4a and 4b show results obtained by K-means algorithm based segmentation of the gray scale version of the Figure 1a, with two predefined values of the interclass distances in the clustering procedure. Figures 4c and 4d shows result obtained by applying ratio imaging method with two threshold levels, 5 and 10, on the fluorescent RGB image shown in Figure 1a. While K-means clustering yielded robust result for different interclass distances, ratio imaging method demonstrated great level of sensitivity with respect to the threshold level that is difficult to define optimally. When K-means algorithm was applied on the gray scale version of the fluorescent RGB image shown in Figure 1b, with the same values for interclass distances as in Figures 4a and 4b, obtained results are shown in Figures 5a and 5b. In direct comparison with Figures 4a and 4b, as well as with Figures 1a and 1d, it is evident that K-means algorithm was not able to yield stable estimate of the tumor class when contrast between tumor and surrounding tissue decreased.

The following set of results demonstrates robustness of DCA algorithms, specifically DCA-HPF algorithm, with respect to intensity fluctuation of the fluorescent RGB images of the BCC. For this purpose we first show in Figures 6a to 6c the BCC spatial maps extracted from Figures 1a to 1c by means of the EFICA algorithm [42]. Evidently, the contrast between BCC and surrounding tissue fluctuates and it is impossible to define a single

threshold in order to calculate tumor demarcation line. On the contrary, BCC spatial maps shown in Figures 7a to 7c, that are extracted from Figures 1a to 1c by means of DCA-HPF algorithm, exhibit good contrast between BCC and surrounding tissue. This enables to define a unique threshold set to 0.5. Demarcation lines calculated by means of Canny's edge extraction algorithm from Figures 7a to 7c, with threshold set to 0.5, are superimposed on the gray scale version of the original fluorescent RGB images and shown in Figures 8a to 8c. In direct comparison with Figures 1a and 1d it is evident that demarcation line remains stable, apart from the fact that line on Figure 8c is slightly affected by the noise. It is however important to emphasize that DCA-HPF algorithm delivered stable estimate of the demarcation line when intensity of the fluorescence image varied almost two orders of magnitudes. To further support this statement we show in Figure 9 length of demarcation lines estimated by NMF and DCA algorithms for different levels of the intensity of the illuminating light. Demarcation lines from ICA extracted spatial maps of the BCC were not calculated due to the fact that the results obtained with a fixed threshold set to 0.5 were extremely poor.

To provide further arguments for robustness of the proposed DCA-based tumor demarcation algorithms we have repeated procedure described above on the fluorescent images of the BCC of the second patient. They are shown in Figures 10a to 10c. BCC spatial maps extracted from RGB images shown in Figures 10a to 10c by means of DCA-HPF algorithm are shown in Figures 11a to 11c. Good contrast between BCC and surrounding tissue is achieved. This enabled to define a unique threshold set to 0.5 when calculating tumor demarcation line by means of Canny's edge extraction algorithm. It is important to emphasize again that DCA algorithms delivered stable estimate of the demarcation line when intensity of the fluorescence image varied almost two orders of magnitude. This is

demonstrated in Figure 12 where lengths of demarcation lines estimated by NMF and DCA algorithms are shown for different levels of the intensity of the illuminating light.

Although with the low computational complexity among compared methods, DCA HPF algorithm exhibited good performance in terms of the robustness of the estimated demarcation lines. In the case of first patient the mean value of length of the demarcation line extracted by DCA HPF algorithm was 1427.2 pixels with a standard deviation of 150 pixels. DCA WT algorithm yields mean value of 1724.1 pixels and standard deviation of 745.6 pixels. In the case of second patient the mean value of length of the demarcation line extracted by DCA HPF algorithm was 462.43 pixels with a standard deviation of 33 pixels. DCA WT algorithm yields mean value of 448.29 pixels and standard deviation of 23.27 pixels.

Computation times were estimated on the RGB image shown in Figure 1a with the size of 500×700 pixels, in MATLAB environment on a 2.4 GHz Intel Core 2 Quad Processor Q6600 based desktop computer with 4GB RAM. They are respectively given for the HPF, WT, Inn and SO NMF algorithms as follows: 8.1s, 7.8s, 15.5s and 10s. In the implementation of the innovation-based DCA algorithm a 10th order linear prediction filter has been used.

4. Discussion

The fluorescence contrast between the tumor and normal skin is of essential importance for the reliable demarcation of the tumor tissue from the normal skin by means of PDD. This implies low variation of the intensity of the fluorescence image of the ALA treated normal skin, [3]. However, variation of the fluorescence intensity may be caused by the variation of several factors, either individually or combined: duration of the ALA application time, quality/concentration of the ALA cream and/or intensity of the illuminating light. Hence, in the conducted study we have presented novel approach for robust tumor demarcation:

unsupervised image segmentation methods the performance of which remains invariant under wide range of the variability of the fluorescence intensity. The approach exploits spectral and spatial diversities between the tumor and the surrounding skin in the recorded fluorescent multi-spectral RGB image. It is based on the recent extension of the ICA theory known under the common name of DCA. DCA is necessary to account for statistical dependence among the spatial maps of the tumor and surrounding tissue. Statistical dependence is caused by spectral similarity between the tumor and surrounding tissue due to the coarse spectral resolution of the RGB image as well as due to the deviation of discussed variables from their optimal values. Unlike several state-of-the art image segmentation methods, proposed DCA approach to tumor demarcation exhibited robust performance when intensity of the fluorescence has been varied almost two orders of magnitude. Such high level of robustness is a consequence of the scale invariance property of the used family of DCA algorithms. We conjecture that DCA in combination with multi-spectral imaging systems may represent a good solution for a portable optical detection system which does not require calibration and can be operated easily. This should lay down foundation for the design of the autonomous systems capable for robust calculation of the tumor demarcation lines in the real world clinical conditions.

5. Abbreviations

ALA	δ -5 aminolaevulinic acid
BCC	basal cell carcinoma
BSS	blind source separation
DC	direct current
DCA	dependent component analysis
HPF	High-pass filter

ICA	independent component analysis
Inn	Innovation
NMF	non-negative matrix factorization
PDD	photodynamic diagnosis
PDT	photodynamic therapy
Pp IX	protoporphyrin IX
RGB	red-green-blue
SLMM	Static linear mixture model
WT	wavelet transform

Acknowledgements

The work of I. Kopriva and A. Peršin has been supported through grant 098-0982903-2558. The work of N. Puizina-Ivić and L. Mirić has been supported through grant 141-2180056-0481. Both grants were funded by the Ministry of Science, Education and Sports, Republic of Croatia.

References

- [1] B. Stenquist, M.B. Ericson, C. Strandeberg, L. Mölne, A. Rosén, O. Larkö, A.M. Wennberg, Bispectral fluorescence imaging of aggressive basal cell carcinoma combined with histopathological mapping: a preliminary study indicating a possible adjunct to Mohs micrographic surgery, *British J. of Dermatology* 154 (2006) 305-309.
- [2] D.R. English, B.K. Armstrong, A. Kicker, C. Fleming, Sunlight and cancer, *Cancer Causes Control* 8 (1997) 271-283.

- [3] M.B. Ericson, C. Sandberg, F. Gudmundson, A. Rosén, O. Larkö, A.M. Wennberg, Fluorescence contrast and threshold limit: implications for photodynamic diagnosis of basal cell carcinoma, *J. Photochem. Photobiol. B: Biol.* 69 (2003) 121-127.
- [4] D. Kessel (Ed.), *Methods in Porphyrin Photosensitisation, Advances in Experimental Medicine and Biology*, Vol. 193, Plenum, New York, 1985, p. 352.
- [5] J. C. Kenedy, R. H. Pottier, Endogenous protoporphyrin IX, a clinically useful photosensitizer for photodynamic therapy, *J. Photochem. Photobiol. B: Biol.* 14 (1992) 275-292.
- [6] S. Andersson-Engels, R. Berg, K. Svanberg, S. Svanberg, Multi-colour fluorescence imaging in connection with photodynamic therapy of delta-amino levulinic acid (ALA) sensitised skin malignancies, *Bioimaging* 3 (1995) 134-143.
- [7] Q. Peng, T. Warloe, K. Berg, J. Moan, M. Kongshaug, K. E. Giercksky, J. M. Nesland, 5-Aminolevulinic acid-based photo-dynamic therapy: clinical research and future challenges, *Cancer* 79 (1997) 2282-2308.
- [8] H. Heyerdhal, I. Wang, D.L. Liu, R. Berg, S. Andersson-Engels, Q. Peng, J. Moan, S. Svanberg, Pharmacokinetic studies on 5-aminolevulinic acid-induced protoporphyrin IX accumulation in tumors and normal tissues, *Cancer Lett.* 112 (1997) 225-231.
- [9] C. Fritsch, N.J. Neuman, T. Ruzicka, P. Lehmann, Photodiagnostic test. 3: Fluorescence diagnosis with delta-aminolevulinic acid-induced porphyrins (FDAP) in dermatology, *Hautarzt* 51 (2000) 528-543, quiy 543-525.
- [10] F. Koenig, J. Knittel, H. Stepp, Diagnostic Cancer in Vivo, *Science* 292 (2001) 1401-1403.
- [11] M.A. Scott, C. Hopper, A. Sahota, R. Springett, B.W. McIlroy, S.G. Bown, A.J. MacRobert, Fluorescence Photodiagnostics and Photobleaching Studies of Cancerous

Lesions using Ratio Imaging and Spectroscopic Techniques, *Lasers Med Sci* 15 (2000) 63-72.

[12] W. Bäuml, C. Abels, R.M. Szeimies, Fluorescence Diagnosis and Photodynamic Therapy in Dermatology, *Med. Laser Appl.* 18 (2003) 47-56.

[13] F. Fischer, E.F. Dickson, R.H. Pottier, H. Wieland, An Affordable, Portable Fluorescence Imaging Device for Skin Lesion Detection Using a Dual Wavelength Approach for Image Contrast Enhancement and Aminolaevulinic Acid-induced Protoporphyrin IX. Part. I Design, Spectral and Spatial Characteristics, *Lasers Med Sci* 16 (2001) 199-206.

[14] F. Fischer, E.F. Dickson, J.C. Kennedy, R.H. Pottier, An Affordable, Portable Fluorescence Imaging Device for Skin Lesion Detection Using a Dual Wavelength Approach for Image Contrast Enhancement and Aminolaevulinic Acid-induced Protoporphyrin IX. Part II. In Vivo Testing, *Lasers Med Sci* 16 (2001) 207-212.

[15] A. Ehrhardt, H. Stepp, K.M. Irion, W. Stummer, D. Zaak, R. Baumgartner, A. Hofstetter, Fluorescence Detection of Human Malignancies Using Incoherent Light Systems, *Med. Laser Appl.* 18 (2003) 27-35.

[16] J. Hewett, V. Nadeau, J. Ferguson, H. Moseley, S. Ibbotson, J.W. Allen, W. Sibbett, M. Padgett, The Application of a Compact Multispectral Imaging System with Integrated Excitation Source to *In vivo* Monitoring of Fluorescence During Topical Photodynamic Therapy of Superficial Skin Cancers, *Photochem. Photobiol.* 73 (2001) 278-282.

[17] I. Kopriva, A. Peršin, H. Zorc, A. Pašić, J. Liopozenčić, K. Kostović, M. Lončarić, Visualisation of basal cell carcinoma by fluorescence diagnosis and independent component analysis, *Photodiagnosis and Photodynamic Therapy* 4 (2007) 190-196.

[18] L. Xu, M. Jackowski, A. Goshtasby, D. Roseman, S. Bines, C. Yu, A. Dhawan, A. Huntley, Segmentation of skin cancer images, *Image Vision and Computing* 17 (1999) 65-74.

- [19] J. Zhang, C.-I. Chan, S.J. Miller, K.A. Kang, A feasibility study of multispectral image analysis of skin tumors, *Biomed. Inst. and Techn.* 34 (2000) 275-282.
- [20] K. Tabatabaie, A. Esteki, Independent Component Analysis as an Effective Tool for Automated Diagnosis of Melanoma, in: *Proceedings of the IEEE Biomedical Engineering Conference (CIBEC'08)*, 2008, pp. 1-4.
- [21] S. G. Kong, L. J. Park, Hyperspectral Image Analysis for Skin Tumor Detection, Chapter 7 in: R.I. Hamond (Ed.), *Augmented Vision Perception in Infrared: Algorithms and Applied Systems*, *Advances in Pattern Recognition*, Springer Verlag, London, 2009, pp. 155-171.
- [22] M. Elbaum, A.W. Kopf, H.S. Rabinovitz, R.G.B. Langley, H. Kamino, M.C. Mihm, A.J. Sober, G.L. Peck, A. Bogdan, D. Gutkowitz-Krusin, M. Greenebaum, S. Keem, M. Oliviero, S. Wang, Automatic differentiation of melanoma from melanocytic nevi with multispectral digital dermoscopy: A feasibility study, *J. Am. Acad. Dermatol.* 44 (2001) 207-218.
- [23] A. Hyvärinen, J. Karhunen, E. Oja, *Independent Component Analysis*, Wiley Interscience, 2001.
- [24] A. Cichocki, S. Amari, *Adaptive Blind Signal and Image Processing*, John Wiley, New York, 2002.
- [25] Q. Du, I. Kopriva, H. Szu, Independent Component Analysis for Hyperspectral Remote Sensing, *Opt. Eng.* 45 (2006) 017008-1-13.
- [26] Q. Du, I. Kopriva, H. Szu, Independent Component Analysis for Classifying Multispectral Images with Dimensionality Limitation, *Int. J. Inf. Acq.* 1 (2004) 201-216.
- [27] L. Parra, K.-R. Mueller, C. Spence, A. Ziehe, P. Sajda, Unmixing hyperspectral data, *Advances in Neural Information Processing Systems* 12 (2000) 942-948.
- [28] C. Caiafa, E. Salerno, A. Proto, L. Fiumi, Blind spectral unmixing by local maximization of non-Gaussianity, *Sig. Proc.* 88 (2008) 50-68.

- [29] J. M. P. Nascimento, J. M. B. Dias, Unmixing Hyperspectral Data: Independent and Dependent Component Analysis, in: *Hyperspectral Data Exploitation: Theory and Applications*, C.I. Chang, Ed. New York, John Wiley, 2007, pp. 149-177.
- [30] A.K. Barros, in: M. Girolami (Ed.), *Advances in Independent Component Analysis*, Springer, 2000, pp. 63-71.
- [31] A. Hyvärinen, Independent component analysis for time-dependent stochastic processes, in: *Proceedings of the International Conference on Artificial Neural Networks (ICANN'98)*, 1998, pp. 541-546.
- [32] N. Bonnet, D. Nuzillard, Independent component analysis: A new possibility for analyzing series of electron energy loss spectra, *Ultramicroscopy* 102 (2005) 327-337.
- [33] I. Kopriva, D. Seršić, Wavelet Packets Approach to Blind Separation of Statistically Dependent Sources, *Neurocomputing* 71 (2008) 1642-1655.
- [34] I. Kopriva, D. Seršić, Robust Blind Separation of Statistically Dependent Sources Using Dual Tree Wavelets, in: *Proceedings of the 2007 IEEE International Conference on Image Processing*, 2007, pp. 433-436.
- [35] A. Cichocki, P. Georgiev, Blind source separation algorithms with matrix constraints, *IEICE Trans. on Fund. of Electr., Comm. and Comp. Sci.* E86-A (2003) 522-531.
- [36] T. Tanaka, A. Cichocki, Subband decomposition independent component analysis and new performance criteria, in: *Proceedings of the IEEE Conference Acoustics, Speech and Signal Processing*, 2004, pp. 541-544.
- [37] A. Cichocki, General component analysis and blind source separation methods for analyzing multichannel brain signals, in: *Statistical and Process Models of Cognitive Aging*, J. Wenger, M. Schuster, C.(Eds.), Notre Dame Series on Quantitative Methods , Erlbaum, Mahwah, NJ, 2007.

- [38] J.B. Adams, M.O. Smith, Spectral mixture modeling: A new analysis of rock and soil types at the Viking Lander 1 suite, *J. of Geophys. Res.* 91 (1986) 8098–8112.
- [39] J.B. Adams, M.O. Smith, A.R. Gillespie, Image spectroscopy: Interpretation based on spectral mixture analysis, in: C. M. Pieters, P. A. Englert (Eds.), *Remote Geochemical Analysis: Elemental and Mineralogical Composition*, Cambridge University Press, 1993, pp. 145–166.
- [40] J.J. Settle, N.A. Drake, Linear mixing and estimation of ground cover proportions, *Int. J. of Remote Sensing* 14 (1993) 1159–1177.
- [41] C.-I. Chang, S.-S. Chiang, J.A. Smith, I.W. Ginsberg, Linear spectral random mixture analysis for hyperspectral imagery, *IEEE Trans. on Geosc. and Rem. Sens.* 40 (2002) 375–392.
- [42] Z. Koldovský, P. Tichavský, E. Oja, Efficient Variant of Algorithm for FastICA for Independent Component Analysis Attaining the Cramér-Rao Lower Bound, *IEEE Tr. on Neural Networks* 17 (2006) 1265-1277.
- [43] A. Hyvärinen, E. Oja, A fast fixed-point algorithm for independent component analysis, *Neural Computation* 9 (1997) 1483-1492.
- [44] A. Hyvärinen, Fast and robust fixed-point algorithms for independent component analysis, *IEEE Trans. Neural Network* 10 (1999) 626-634.
- [45] D. D. Lee, H. S. Seung, Learning the parts of objects by non-negative matrix factorization, *Nature* 401 (1999) 788-791.
- [46] A. Cichocki, R. Zdunek, S. Amari, Nonnegative Matrix and Tensor Factorization, *IEEE Sig. Proc. Magazine* 25 (2008) 142-145.
- [47] R. Zdunek, A. Cichocki, Nonnegative matrix factorization with constrained second-order optimization, *Sig. Proc.* 87 (2007) 1904-1916.

- [48] P. O. Hoyer, Non-negative Matrix Factorization with Sparseness Constraints, *J. of Mach. Learn. Res.* 5 (2004) 1457-1469.
- [49] M. Kass, A. Witkin, D. Terzopoulos, Snakes: Active Contour Models, *Int. J. Comp. Vis.* 1 (1988) 321-331.
- [50] J. Malik, S. Belongie, T. Leung, J. Shi, Contour and Texture Analysis for Image Segmentation, *Int. J. Comp. Vis.* 43 (2001) 7-27.
- [51] T. Chan, L. Vese, Active contours without edges, *IEEE Trans. Imag. Proc.* 10 (2001) 266-277.
- [52] Ch. Li, Ch. Xu, Ch. Gui, M.D. Fox, Level Set Evolution Without Re-initialization: A New Variational Formulation, in: *IEEE International Conference on Computer Vision and Pattern Recognition*, 2005, pp. 430-436.
- [53] R. Xu, D. Wunsch II, Survey of Clustering Algorithms, *IEEE Trans. Neural Networks* 16 (2005) 645-678.
- [54] C.M. Bishop, *Pattern Recognition and Machine Learning*, Springer, 2006.
- [55] <http://www.mathworks.com/matlabcentral/fileexchange/loadCategory.do>

Figure captions

Figure 1. RGB fluorescent images of the BCC from the first patient acquired under different intensities of illumination: (a) illumination with the maximal intensity I_0 ; (b) illumination with the intensity $I_0/9.15$; illumination with the intensity $I_0/73.47$; (d) RGB fluorescent image with demarcation line manually marked by the red dots.

Note on color reproduction: color reproduction on the Web.

Figure 2. Histograms of the grayscale versions of the RGB color images of the BCC respectively shown in Figures 1a to 1c.

Note on color reproduction: color reproduction on the Web.

Figure 3. Evolution curve after 700 iterations calculated by the level set method [46,49] and superimposed on the gray scale version of the fluorescent RGB image shown in Figure 1a.

Note on color reproduction: color reproduction on the Web.

Figure 4. Segmentation results obtained by: (a) K-means algorithm applied on gray scale version of the Figure 1a for the interclass distance set to 45; (b) similar as (a) but with interclass distance set to 95; (c) ratio imaging method applied on fluorescent RGB image shown in Figure 1a with threshold set to 5; (d) similar as (c) but with threshold set to 10.

Figure 5. Segmentation results obtained by K-means algorithm applied on gray scale version of the Figure 1b for: (a) the interclass distance set to 45; (b) the interclass distance set to 95.

Figure 6. BCC spatial maps in extracted from fluorescent RGB images shown in Figures 1a to 1c by means of EFICA algorithm [36]. Extracted maps are normalized on interval [0, 1] and shown in pseudo-color scale.

Note on color reproduction: color reproduction on the Web.

Figure 7. BCC spatial maps in extracted from fluorescent RGB images shown in Figures 1a, 1b and 1c by means of DCA-HPF algorithm. Extracted maps are normalized on interval [0, 1] and shown in pseudo-color scale.

Note on color reproduction: color reproduction on the Web.

Figure 8. BCC demarcation lines calculated by means of Canny's edge extraction method from spatial maps shown in Figures 7a to 7c, with a fixed threshold set to 0.5. Demarcation lines were superimposed on the gray scale version of the fluorescent RGB images shown in Figures 1a to 1c.

Note on color reproduction: color reproduction on the Web.

Figure 9. Estimated lengths of the demarcation lines in pixels. Demarcation lines were calculated by means of Canny's edge extraction method with a fixed threshold set to 0.5, and from the BCC spatial maps extracted from the fluorescent RGB images by means of NMF

and DCA algorithms. Legend: red circles - DCA HPF algorithm [30,31]; green diamonds - DCA WT algorithm [30]; blue triangles - DCA Inn algorithm [28]; magenta stars - SO NMF algorithm [42].

Note on color reproduction: color reproduction on the Web.

Figure 10. RGB fluorescent images of the BCC from the second patient acquired under different intensities of illumination: (a) illumination with the maximal intensity I_0 ; (b) illumination with the intensity $I_0/12.21$; illumination with the intensity $I_0/58.67$.

Note on color reproduction: color reproduction on the Web.

Figure 11. BCC spatial maps in extracted from fluorescent RGB images shown in Figures 10a to 10c by means of EFICA algorithm [36]. Extracted maps are normalized on interval $[0, 1]$ and shown in pseudo-color scale.

Figure 12. Estimated lengths of the demarcation lines in pixels. Demarcation lines were calculated by means of Canny's edge extraction method with a fixed threshold set to 0.5, and from the BCC spatial maps extracted from the fluorescent RGB images by means of NMF and DCA algorithms. Legend: red circles - DCA HPF algorithm [30,31]; green diamonds - DCA WT algorithm [30]; blue triangles - DCA Inn algorithm [28]; magenta stars - SO NMF algorithm [42].

Note on color reproduction: color reproduction on the Web.

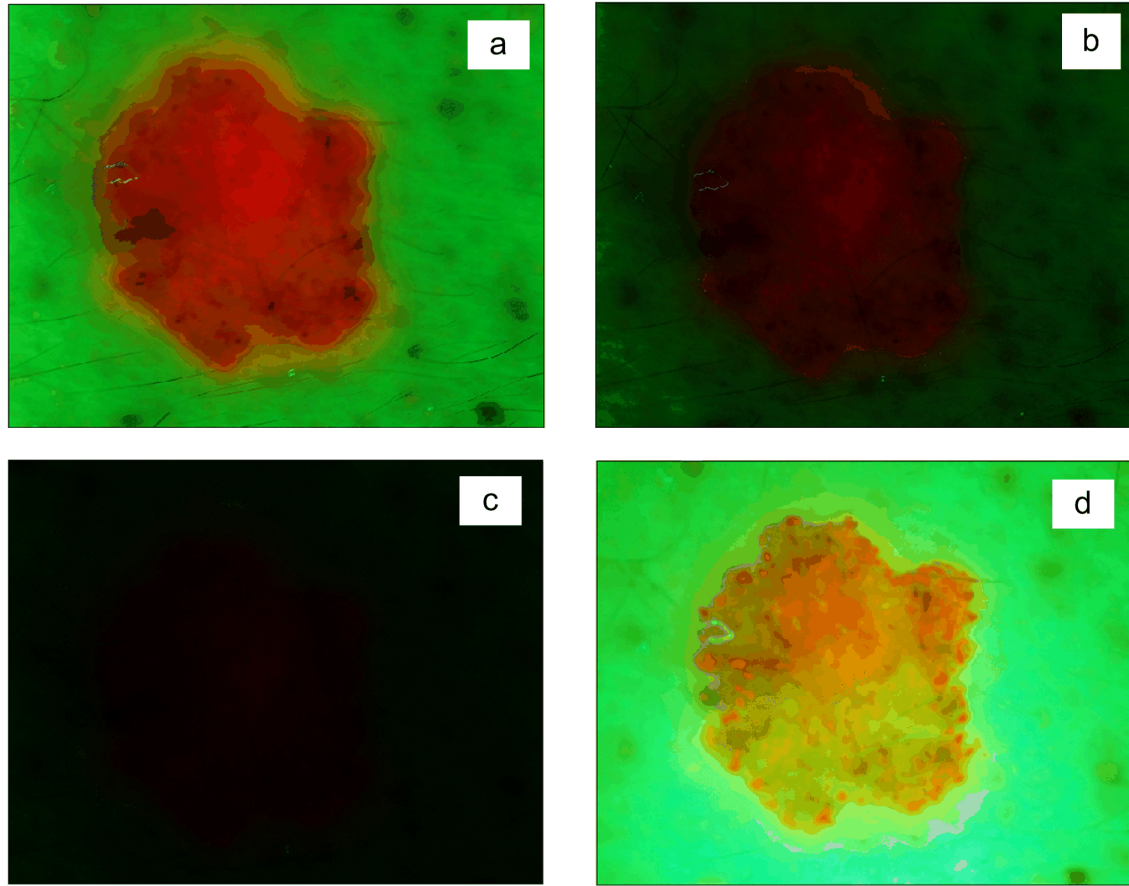


Fig1

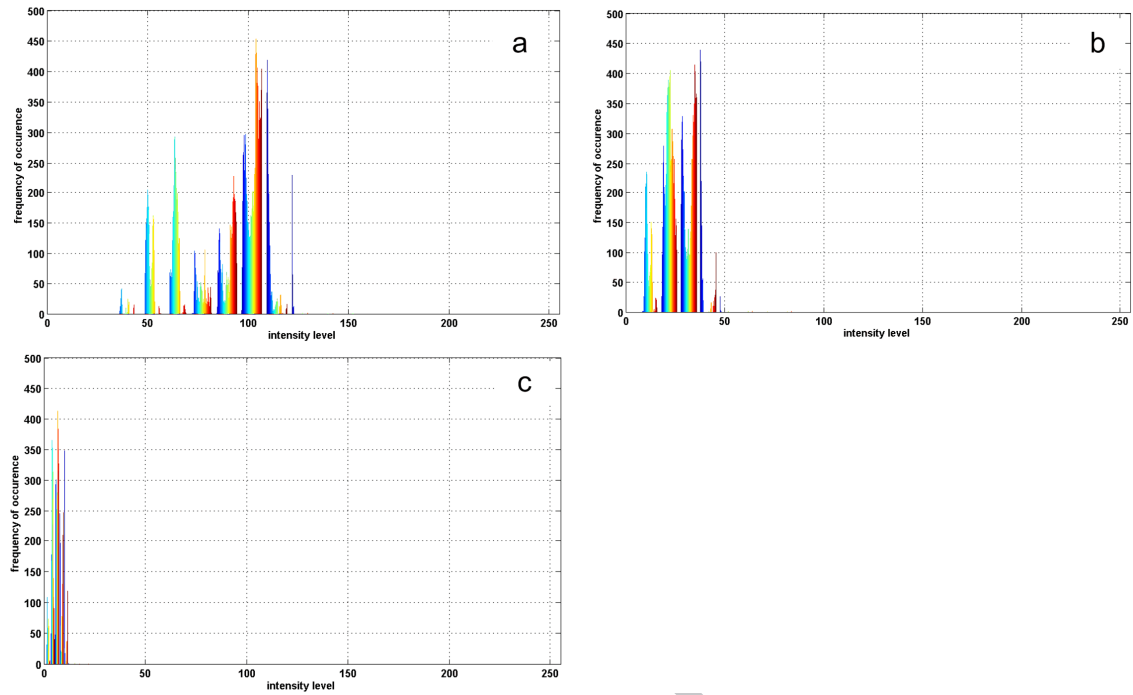


Fig2

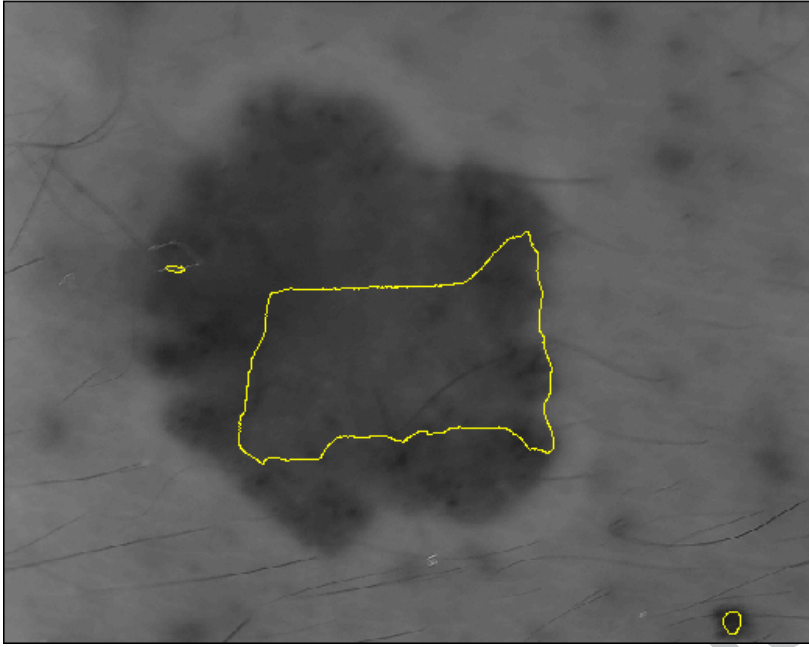


Fig3

ACCEPTED MANUSCRIPT

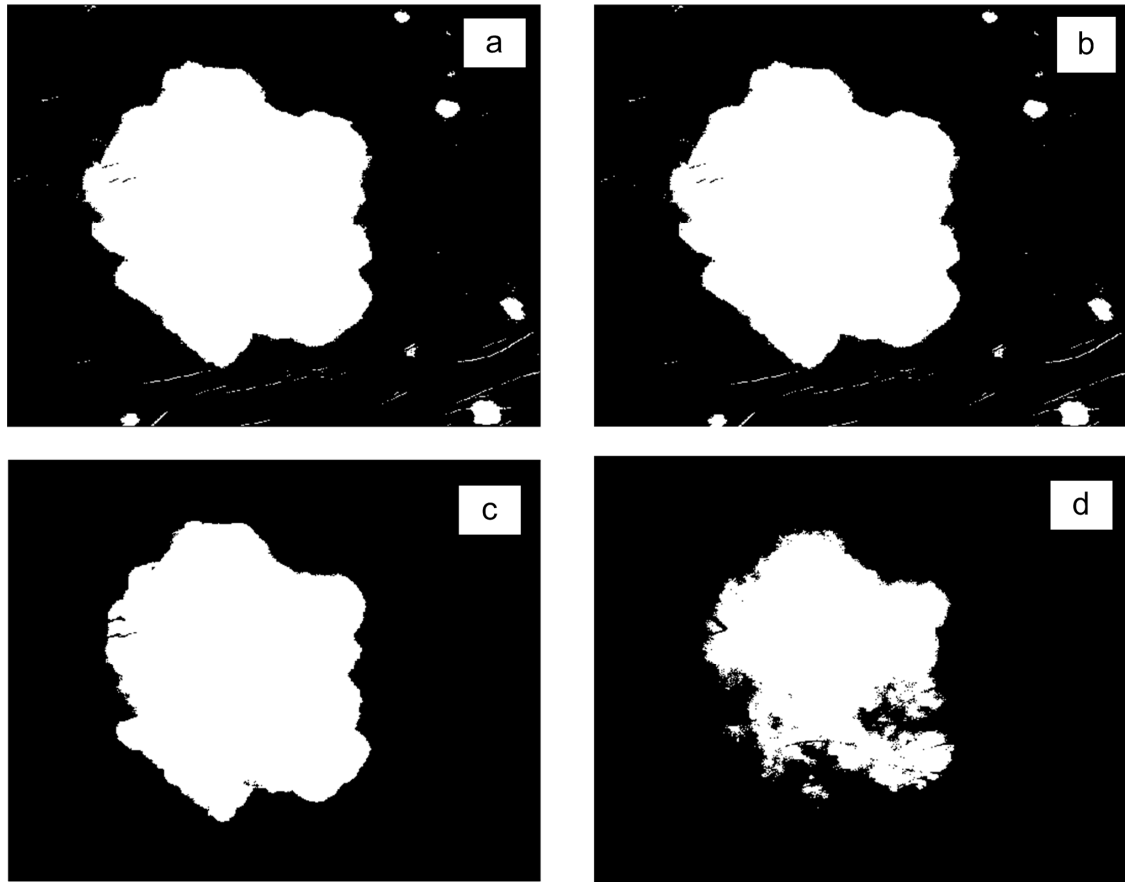


Fig4

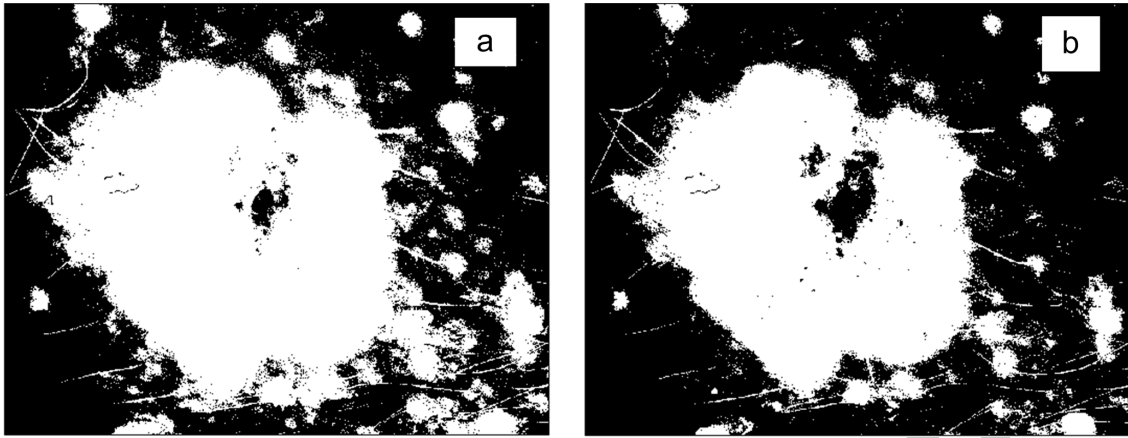


Fig5

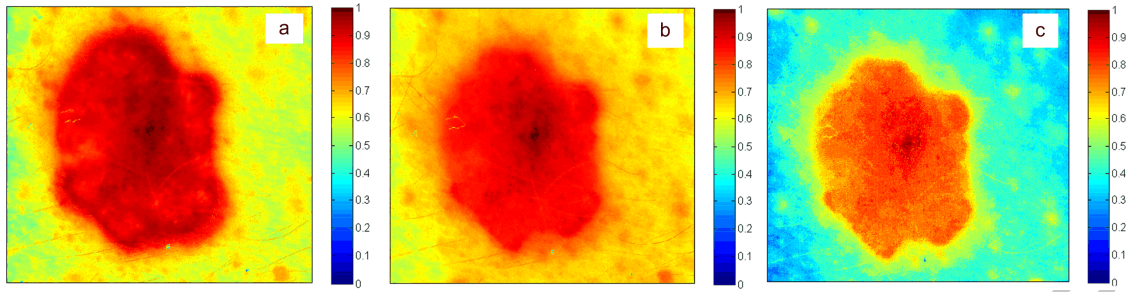


Fig6

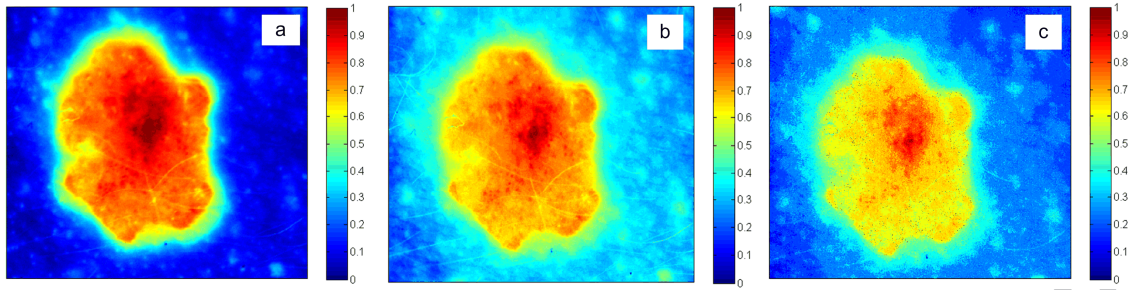


Fig7

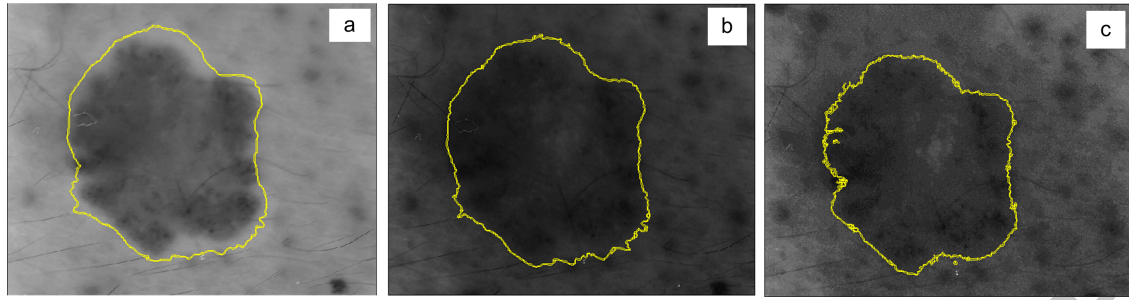


Fig8

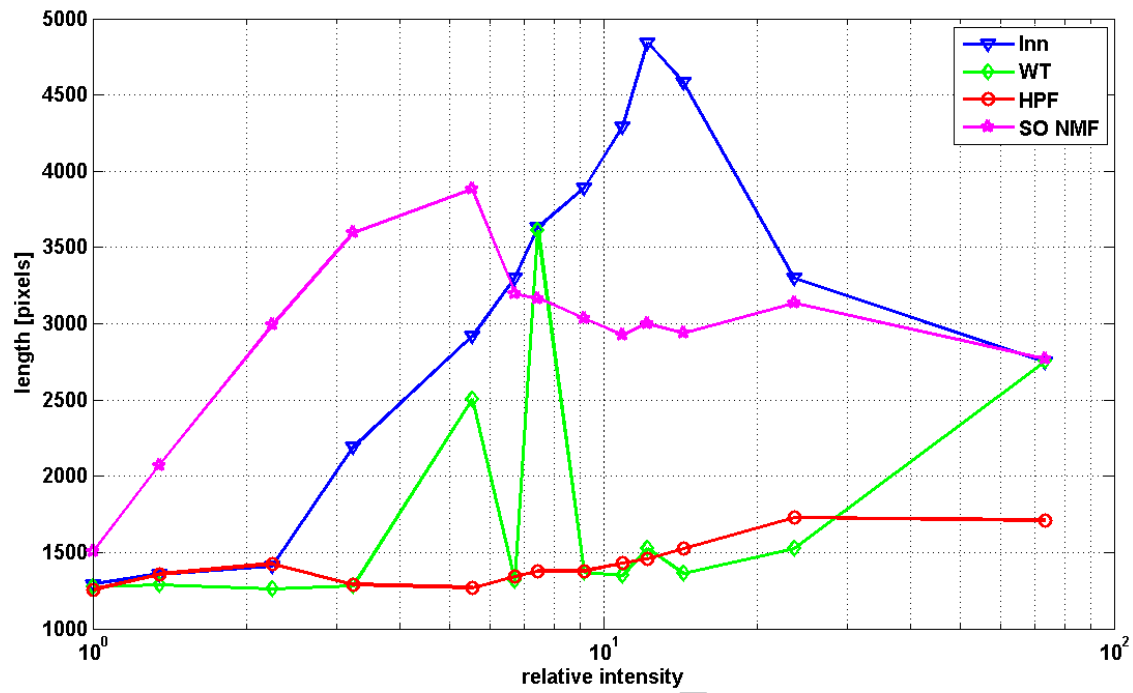


Fig9

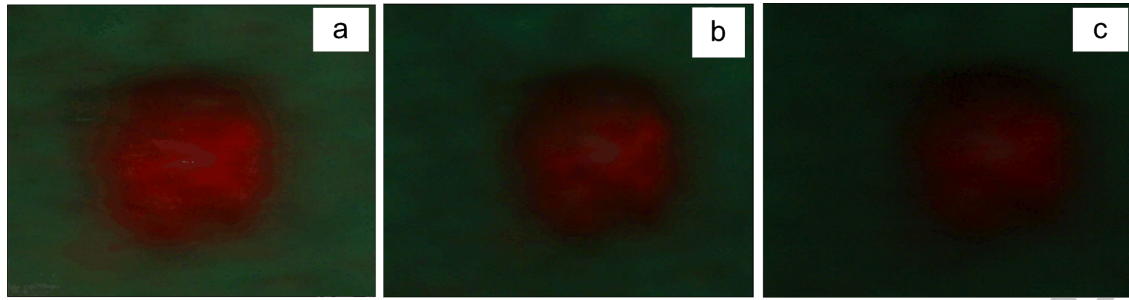


Fig10

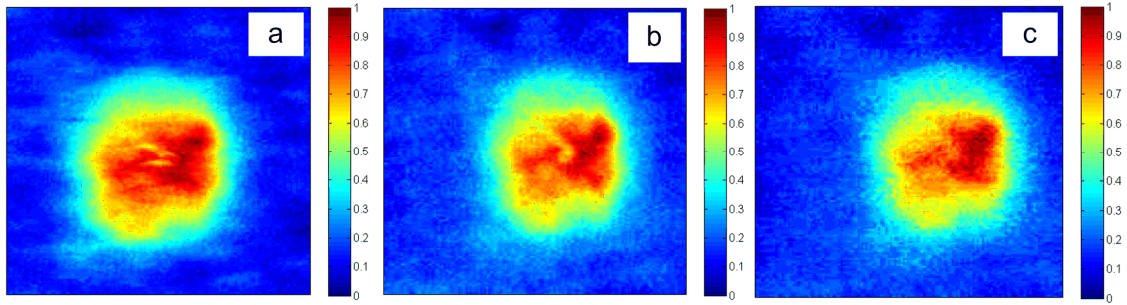


Fig11

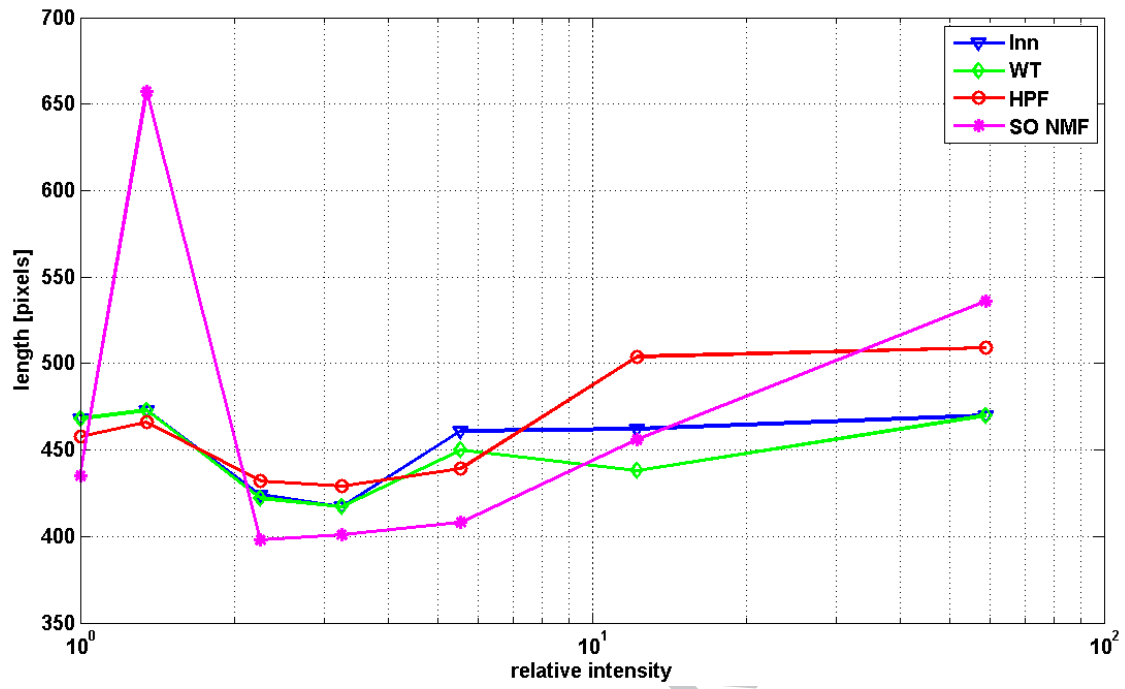


fig12